



Performance Evaluation and Modification Mechanism of Red Clay Treated with Lignosulfonate

Hongyan Ma¹ · Chenglin Pei¹ · Sihan Li¹ · Song Xu¹

Received: 26 January 2024 / Revised: 6 April 2024 / Accepted: 19 April 2024
© The Author(s), under exclusive licence to the Iran University of Science and Technology 2024

Abstract

Red clay exhibits characteristics such as softening owing to water absorption and cracking because of water loss, which can lead to slope instability, road cracking, and compromised structural integrity when used directly in roadbed filling. Although the addition of industrial materials such as cement is a common engineering treatment, it severely impairs soil renewability. Lignosulfonate (LS) extracted from paper plant waste fluids is a natural bio-based polymer with promising applications as a soil improver. In this study, the boundary moisture content and mechanical properties of LS-treated red clay were investigated using Atterberg, unconfined compressive strength, and direct shear strength tests. Additionally, the LS-treated red clay modification mechanism was explored at multiple scales using zeta potential analysis, X-ray diffraction, scanning electron microscopy coupled with energy dispersive spectroscopy, and Fourier transform infrared spectroscopy. The results indicated that the LS dosage significantly affected both the water content and mechanical strength of the red clay boundaries. The optimal dosage of LS for red clay was 3 wt. %, at which the liquid limit was reduced by 32.97%, the plastic limit by 19.33%, and the plasticity index by 48.37%. The 28-day compressive strength of LS-treated red clay was increased by 378.4%, and the direct shear strength was increased by 136%. Analysis of the microstructure and mineral composition revealed that the LS-treated red clay did not form new minerals, but primarily filled pores and connected soil particles. Through the combined effects of hydrogen bonds, electrostatic interactions, and cation exchange, the LS-treated red clay reduced the size of the mineral particles and the thickness of the mineral double electric layer, resulting in increased structural densification. These results are of great scientific significance for the ecological modification of soils.

✉ Song Xu
xusong@fzu.edu.cn

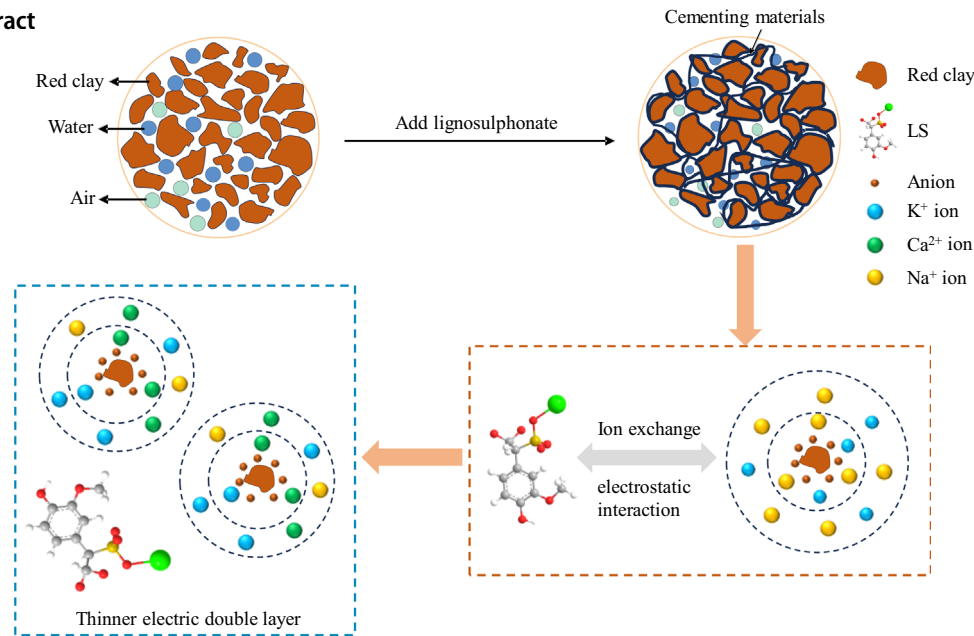
Hongyan Ma
mhyhit@163.com

Chenglin Pei
Uaena30@163.com

Sihan Li
sihanli0112@qq.com

¹ College of Civil Engineering, Fuzhou University, Fuzhou, People's Republic of China

Graphical Abstract



Keywords Red clay · Lignosulfonate · Boundary moisture content · Mechanical property · Microstructure · Modification mechanism

1 Introduction

Red clay is a category of special soil with a high liquid limit ($LL > 50\%$), high plasticity index ($PI > 26$), and fine gradation (clay content $> 90\%$) formed by the weathering of carbonate rocks under subtropical climatic conditions [1–3]. It contains a large amount of hydrophilic clay minerals, exhibits a high natural water content, easy shrinkage and cracking, and poor water stability [3–8]. The Chinese Specifications for Design of Highway Subgrades (JTG D30-2015) [9] stipulate that untreated high-liquid-limit soil cannot be used directly as a roadbed filler to avoid uneven settlement, slope collapse, landslides, and other engineering problems [10, 11].

To solve the problem of high-plasticity clay not being used directly for roadbed filling, geotechnical engineering experts have explored a series of improvement measures to meet the requirements of road construction projects. Modified soils, such as sand and gravel, are commonly used as physical reinforcement [7, 8]. With the rapid advancement of project construction, the demand for construction materials such as sand and stone has increased, resulting in the depletion of sand and stone resources and increasingly serious damage to the natural environment [12]. Therefore, some scholars have attempted to use chemical modifications to solidify soil. The most common

method of stabilizing clay is the addition of cement, lime, or fly ash. Vipulanandan and Mohammed used a polymer solution to treat expansive soil, which reduced the LL and PI [13, 14]. Simultaneously, the nonlinear Vipulanandan p - q stress–strain model was used to simulate the compressive stress–strain relationship between the lime and polymer-treated expansive soil [15–17]. Lime can be mixed with soil using water for cation exchange and flocculation, thereby achieving clay stabilization [18]. Generally speaking, the optimal lime dosage is usually between 1 and 8%, but different soils and conditions may require different optimal lime dosages. The strength of the soil did not increase linearly with increasing lime content. Excessive lime content reduces the maximum strength of soil [18, 19]. It can induce agglomeration and cementation of particles but has a poor curing effect on clays with a higher PI . In addition, lime modification increases the total porosity of the soil and harms its pore structure [20]. Cement can be used to stabilize most soils, including red clays, and the mechanisms by which cement stabilizes soils have been extensively studied [10, 21, 22]. Similar to the lime-modified soil, the curing effect is poor for clay with a high PI [23].

Lignosulfonate (LS) is a bio-based polymer obtained as a byproduct of the paper industry. It is environmentally friendly, does not affect soil or groundwater quality, and

maintains soil ductility while increasing its strength and stiffness [24–26]. Seco et al. found that additives containing cations such as Ca^{2+} and Mg^{2+} reduce the repulsive force between clay layers and induce their flocculation [27]. This flocculation reduces soil plasticity, reduces swelling, and increases the bearing capacity. Canakci et al. discovered that with the addition of 15% lignin, the plastic index of expansive soil decreased by 50%, and the unconfined compressive strength (UCS) increased [28]. Alagzgha et al. studied the effects of different percentages of calcium lignosulfonate (CLS) on the soil. After 2% modification, the free expansion rate and swelling pressure of the soil were reduced by 20% [29]. Recently, Qingsheng et al. found that CLS cements with silt soil improved the mechanical properties and water stability of the modified soils [30]. Zhentao et al. investigated the collapsibility of CLS-modified loess and found that the protonation and ion exchange of CLS reduced the thickness of the double electric layer of soil particles [31]. However, LS has been mainly focused on the strength and mechanical properties of solidified expansive soil, loess, and silt, and there are few studies on the impact of LS on the critical moisture content of red clay [32]. In addition, because of the complexity of LS itself, the improvement mechanism of red clay treated with LS is not as clear as that of traditional stabilizers such as cement, and research on the intrinsic relationship between the microstructure and macroscopic properties after LS modification is also quite limited.

In this study, the mechanical properties and boundary moisture content of modified red clay were examined through the implementation of tests including the Atterberg, UCS, and direct shear. The optimal dosage of LS was determined, and the effect of curing age on the compressive strength and shear strength of modified soil was studied. Additionally, alterations in the microstructure, elemental composition, and mineral composition of LS-treated red clay were analyzed using a scanning electron microscope (SEM) equipped with energy dispersive spectroscopy (EDS), X-ray diffraction (XRD), and Fourier transform infrared (FTIR) spectroscopy to establish the mechanism of change in the mechanical properties and boundary moisture content of LS-treated red clay at multiple scales. The purpose of the experimental research was to provide a new idea for the improvement of high-liquid-limit red clay and replace traditional materials with environmentally friendly and economical materials. The experimental results can provide a reference for practical engineering applications.

2 Materials and Methods

Figure 1 presents a comprehensive flowchart of the LS processing of red clay. This method includes three key stages: (1) obtaining basic physical property indicators of the LS-treated red clay, (2) evaluating the critical moisture content and mechanical properties, and (3) analyzing the microstructure, elemental composition, and mineral composition. These three stages are described in detail in subsequent subsections.

2.1 Red Clay and LS Curing Agent

The soil used in this study (Fig. 2a) was taken from red clay in Sanming City, Fujian Province, which was passed through a 2 mm sieve after being naturally dried. Laboratory tests were conducted to determine the geotechnical properties of the red clay, and the results are listed in Table 1. As shown in Table 1, the red clay was classified as CH based on the Unified Soil Classification System [33]. X-ray fluorescence results of the soil are presented in Table 2; the main mineral compositions of the red clay were SiO_2 , Al_2O_3 , Fe_2O_3 and CaO .

LS as shown in Fig. 2b was obtained from the waste by-product of the processed paper industry mills in Henan Province, China, and the main elements of LS were C, O, Ca, and S. LS are natural polymeric anionic surfactants with phenolic hydroxyl groups as the main functional group as described in the previous literature [34]. The pH of LS solution at a concentration of 1 wt.% was about 6.8 at the temperature of 22 ± 0.5 °C.

2.2 Specimen Preparation

In this study, LS-treated red clay was prepared by mixing a certain amount of LS with red clay. The red clay was naturally dried, crushed, and sifted through a 2 mm mesh to obtain uniform particles. Then the red clay and LS were mixed thoroughly, and a certain amount of deionized water was added to prepare a remoulded soil sample with a water content of 22.8%. The prepared soil specimens were placed in a sealed packet and left to stand at room temperature for 24 h to ensure adequate mixing of soil and moisture. Soil samples for the direct shear strength test were fabricated in a mould with a height of 20 mm and diameter of 61.8 mm after hydrostatic compression, and specimens for UCS test were prepared in a mould with a height of 80 mm and diameter of 39.1 mm. The prepared specimens were wrapped using cling film to prevent water loss, and then placed in a standard conditioning room at a temperature of 20 °C and a relative humidity of 96% for curing until the setting age.

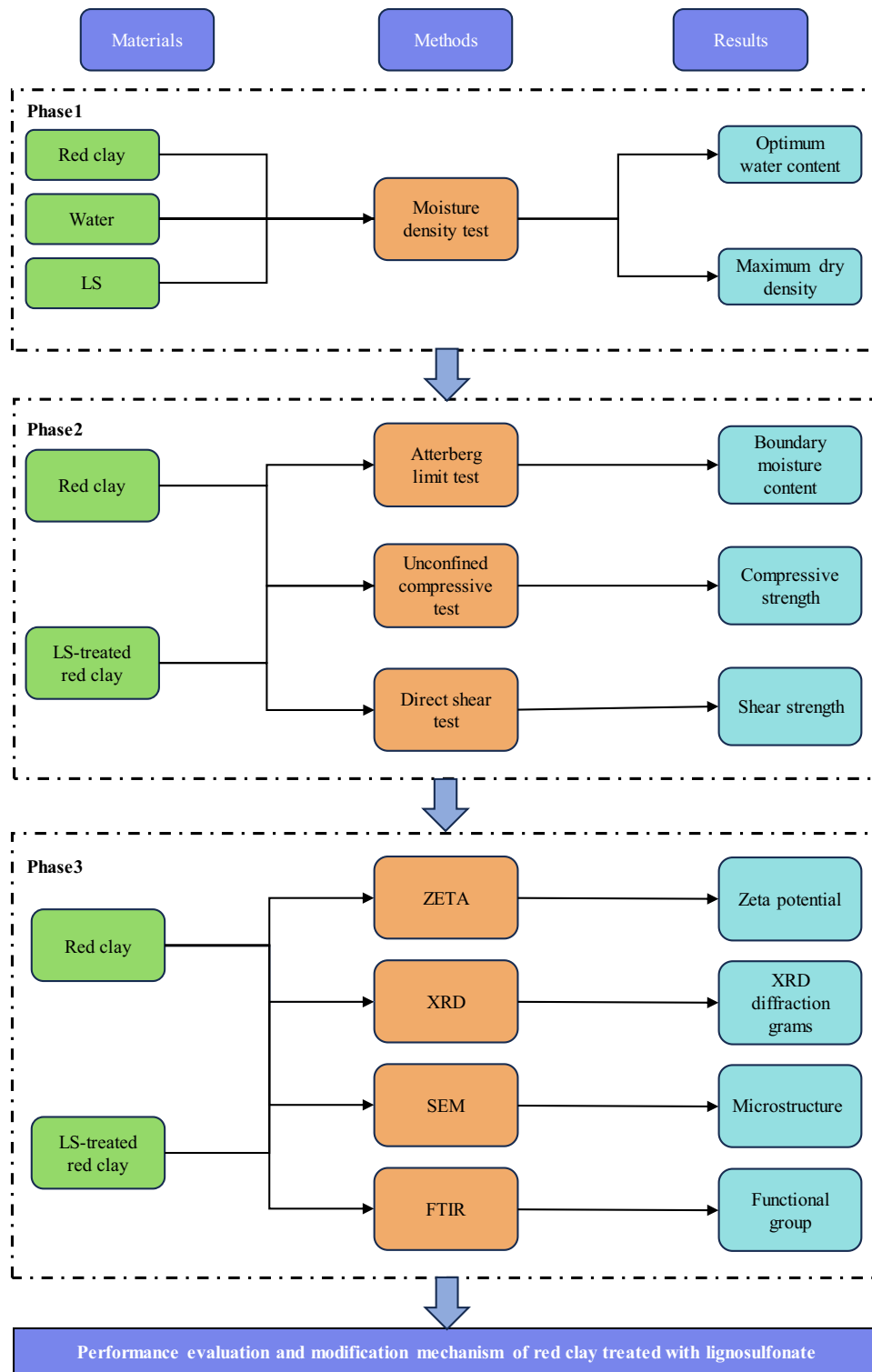


Fig. 1 Flowchart of the performance evaluation and modification mechanism of red clay treated with lignosulfonate (LS)



Fig. 2 Representative specimens of **a** red clay and **b** LS

Table 1 Basic physical indices of red clay

Properties	Values
Natural moisture content (%)	28.5
Liquid limit (%)	65.15
Plasticity limit (%)	34.49
Plasticity index (PI)	30.66
Specific gravity (G_s)	2.76
Maximum dry density ($\text{g}\cdot\text{cm}^{-3}$)	1.543
Optimum moisture content (%)	22.8
pH (water/soil = 1)	4.82
Grain size distribution (%)	
Clay (< 0.005 mm)	31.90
Silt (0.005–0.075 mm)	66.50
Sand (0.075–2.000 mm)	1.60

Table 2 Chemical composition of red clay

Chemical composition (%)	Red clay	Treated (LS = 3 wt.%) red clay
SiO ₂	43.67	39.14
Al ₂ O ₃	22.13	23.35
Fe ₂ O ₃	14.32	16.02
MgO	1.43	1.76
CaO	0.12	7.53
Na ₂ O	0.15	0.18
K ₂ O	2.87	1.82
MnO	0.05	0.05
P ₂ O ₅	0.13	0.17
TiO ₂	1.87	2.11
Others	13.26	7.87

2.3 Measurements

2.3.1 Atterberg Limit

In this test, 200 g of air-dried soil was sieved with 0.5 mm mesh, and then deionized water was added into the soil,

which was put into double-layer preservation bags for 24 h of rest [35]. The liquid and plastic limits of soil samples with LS contents of 0.5 wt.%, 1 wt.%, 3 wt.%, 5 wt.% and 7 wt.% were determined by a photoelectric liquid-plastic limit combined measuring instrument (Fig. 3a). The LS dosage was obtained from literature research and pre-experimentation [36, 37], where 0.5 wt.% dosage was used to better investigate the change in properties of red clay treated with LS between 0 and 1 wt.%. If the test results met the requirements, the soil specimens were put into an oven at a temperature of 105 °C for 8 h and their moisture content was measured to calculate the boundary moisture content of the red clay at each LS dosage.

2.3.2 Direct Shear Strength

The sample for the direct shear strength test was cured in a standard conditioning room for 7, 14 and 28 d. The test was performed on a direct shear apparatus (see Fig. 3b) referring to the ASTM D3080 [38]. Overlying loads of 100, 200, 300 and 400 kPa were applied. The ring cutter was carefully inserted into the shear box, and stress was applied by controlling the equipment to maintain a constant shear rate of 0.8 mm/min. The peak stress was recorded as the shear strength S of the sample. If no peak stress was observed, the experiment was terminated when the shear displacement reached 6 mm, and the shear stress corresponding to 4 mm was recorded as shear strength S .

2.3.3 UCS

The UCS of the LS-treated red clay cured for 7, 14 and 28 d was tested using a pressure testing machine (model: YYW-2, see Fig. 3c) according to ASTM D2166 [39]. The stress and strain of the specimens were measured at 15-s intervals throughout the testing, with the loading rate maintained at 1 mm/min.

2.3.4 Zeta Potential

A nanoparticle size potential analyzer (model: NanoPlus 3, see Fig. 3d) was used to investigate the changes in the thickness of a diffuse double-layer (DDL) of red clay under the influence of LS analyze the mechanism of the change in the boundary moisture content of red clay from the perspective of the diffusion layer. The specific steps for specimen preparation were as follows: The red clay crushed by the straight shear test was dried and pass through 0.075 mm sieve. A total of 1 g red clay was weighed and mixed with 20 ml of ultrapure water to form a suspension, and 10 ml of the upper clarified layer was collected after 30 min of standing. The clear liquid was submitted to the

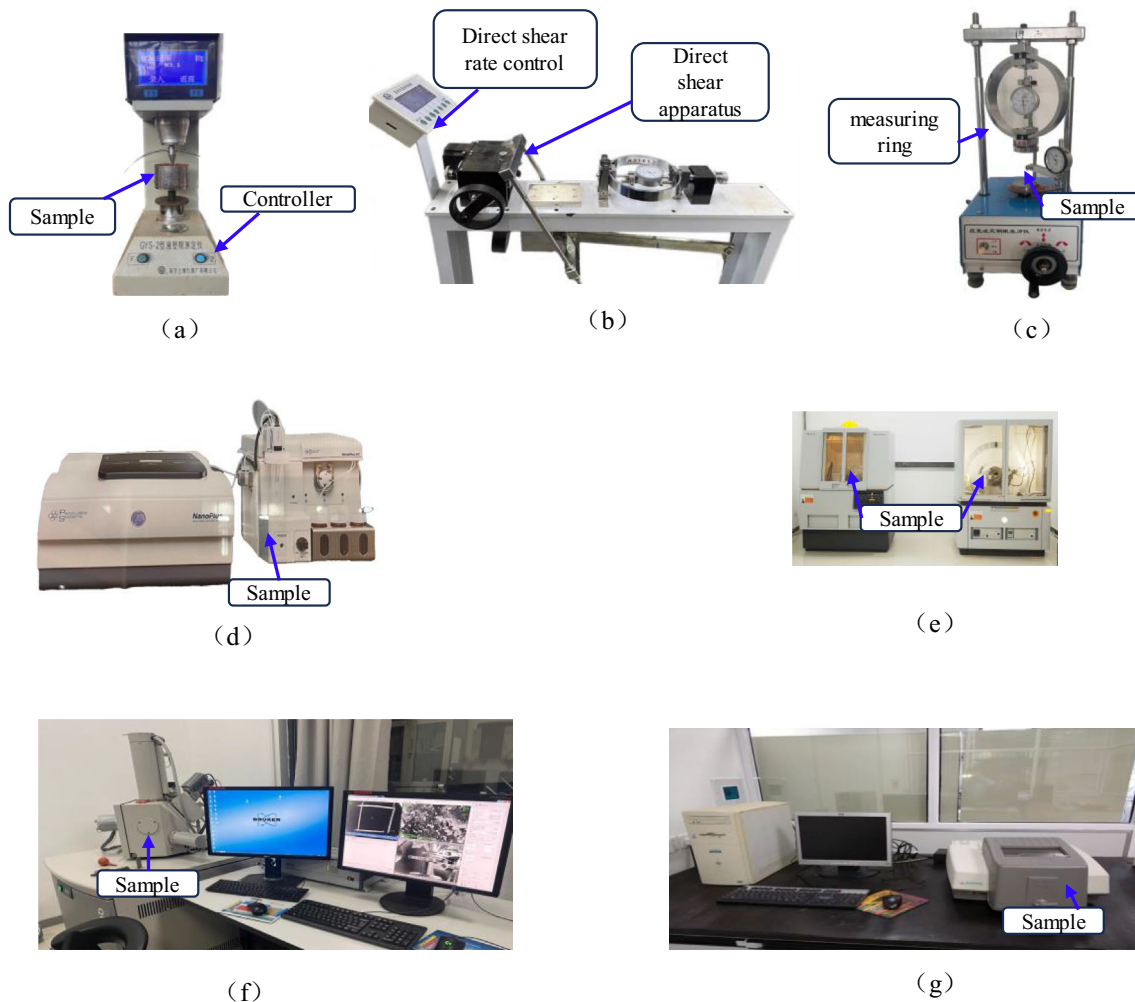


Fig. 3 Test instrument: **a** photoelectric liquid-plastic limit combined measuring instrument, **b** direct shear instrument, **c** unconfined compressive instrument; **d** nanoparticle size potential analyzer instrument, **e** X-ray diffractometer (XRD) instrument, **f** scanning electron microscope (SEM) instrument and **g** Fourier transform infrared (FTIR) spectroscopy instrument

analyzer for determine the zeta potential at temperature of 22 °C [40].

2.3.5 XRD Analysis

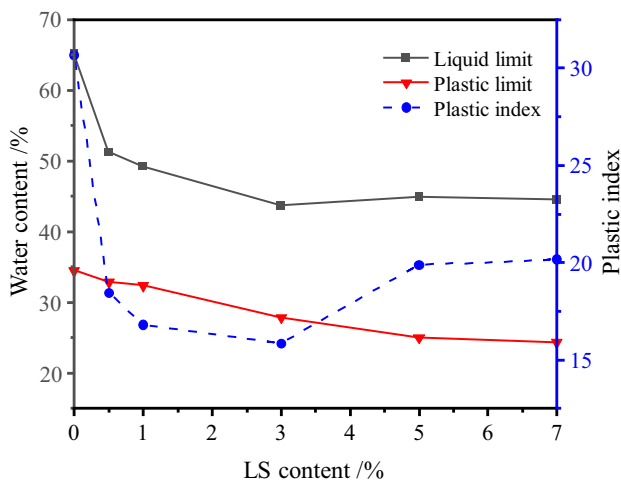
The 3 wt.% LS-treated red clay at the age of 28 days was dried in an oven at 40 °C for 48 h and then passed through 0.075 mm sieve, and analyzed by using XRD (model: X'pert3, see Fig. 3e) with Cu-K α radiation ($\lambda = 0.15405$ nm) at a voltage of 40 kV and current of 20 mA. The scanning range was 10°–80° with a step size of 0.02° and a scanning speed of 2°/min [41]. The test data were processed using MDI Jade 6.5 software, in which the peaks were labelled using standard PDF cards, and the mineral type was determined from the diffraction peaks.

2.3.6 SEM Test

SEM images were captured using an environmental SEM (model: FEI Quanta 250, see Fig. 3f). A specimen of 10 × 10 × 10 mm with naturally formed fracture was extracted from the middle of untreated and 3 wt.% LS-treated red clay after drying for 48 h at 40 °C. Prior to the test, the specimens were coated with a thin gold layer using ion-sputtering equipment to achieve optimal electrical conductivity. The morphology of the specimen was observed using SEM at a magnification of 2,000 times. To quantitatively identify the elemental composition of the modified red clay, elemental analysis was conducted using an EDS [42].

Table 3 Test schema of this work

Test type	Test method	LS Additive content (%)	Compaction degree (%)	Moisture content (%)	Curing time (days)
Atterberg limits	ASTM D4318	0, 0.5, 1, 3, 5, 7	N/A	N/A	1
Direct shear test	ASTM D3080	0, 0.5, 1, 3, 5, 7	95	22.8	7, 14, 28
UCS	ASTM D2166	0, 0.5, 1, 3, 5, 7	95, 97	22.8	7, 14, 28
Zeta	ASTM E2865	0, 0.5, 1, 3, 5, 7	95	22.8	7
SEM	ASTM E986	0, 0.5, 1, 3, 5, 7	95	22.8	28
EDS	ASTM E986	0, 3	95	22.8	28
XRD	ASTM E2860	0, 3	95	22.8	28
FTIR	ASTM E3085	0, 3	95	22.8	28

**Fig. 4** Variation trend of the boundary moisture content

2.3.7 FTIR Spectroscopy

An FTIR spectrometer (model: Nicolet iS50, see Fig. 3g) was used to determine the characteristic functional groups of LS-treated red clay. Prior to the test, 5 g of red clay was dried at 40 °C for 8 h, ground, and passed through a sieve of 0.075 mm. The FTIR spectrum of red clay was recorded within the wavenumber range of 4000–400 cm^{-1} , the number of scans was 64 and the spectral resolution was 4 cm^{-1} [43].

In summary, the details of the test schema are presented in Table 3.

3 Experimental Results and Discussion

3.1 Boundary Moisture Content

The results of the bounding moisture content test for red clay with different LS dosages are shown in Fig. 4. It can be observed from Fig. 4 that the LL and PI of high-liquid-

limit red clay first decreased and then increased with increasing dosages of LS, whereas the plastic limit decreased significantly. The slopes of the curves for both the LL and PI were maximized when the dosage was 0.5 wt.%, and the change in the bounding moisture content is the most obvious and fastest reduction. The LL and PI curves increased slightly when the dosage exceeded 3 wt.%, which indicates that the increase of LS dosage had less and less effect on the boundary moisture content of the red clay. In addition, the LL and PI of the red clay mixed with more than 1 wt.% LS were less than 50% and 26, respectively, which did not belong to the category of high-liquid-limit soils, and indicated that the treatment effect of LS on the high-liquid-limit characteristics of red clay is satisfactory.

3.2 Direct Shear Strength

The results of the direct shear tests on soils with various LS dosages at different curing ages are shown in Fig. 5. The strength of the treated soil increased and subsequently decreased when the LS dosage increased. The shear strength and curing time were positively correlation at a given LS content. The improved direct shear strength is due to the LS modifier, which enhances the interparticle connections, forms larger skeletal aggregates in the soil over time, and is maintained [44]. In addition, shown in Fig. 5c, the LS-treated red clay with 3 wt.% doping has the best reforming effect at the age of 28 d and the vertical load of 400 kPa, which is 58.67% greater than that of the untreated soil. A diagram of a direct shearing specimen is shown in Fig. 6.

3.3 UCS

The effects of the LS dosage and curing time on the UCS values of the specimens under different compaction degrees are illustrated in Fig. 7. It is observed from Fig. 7 that the strength gradually increases with extended curing

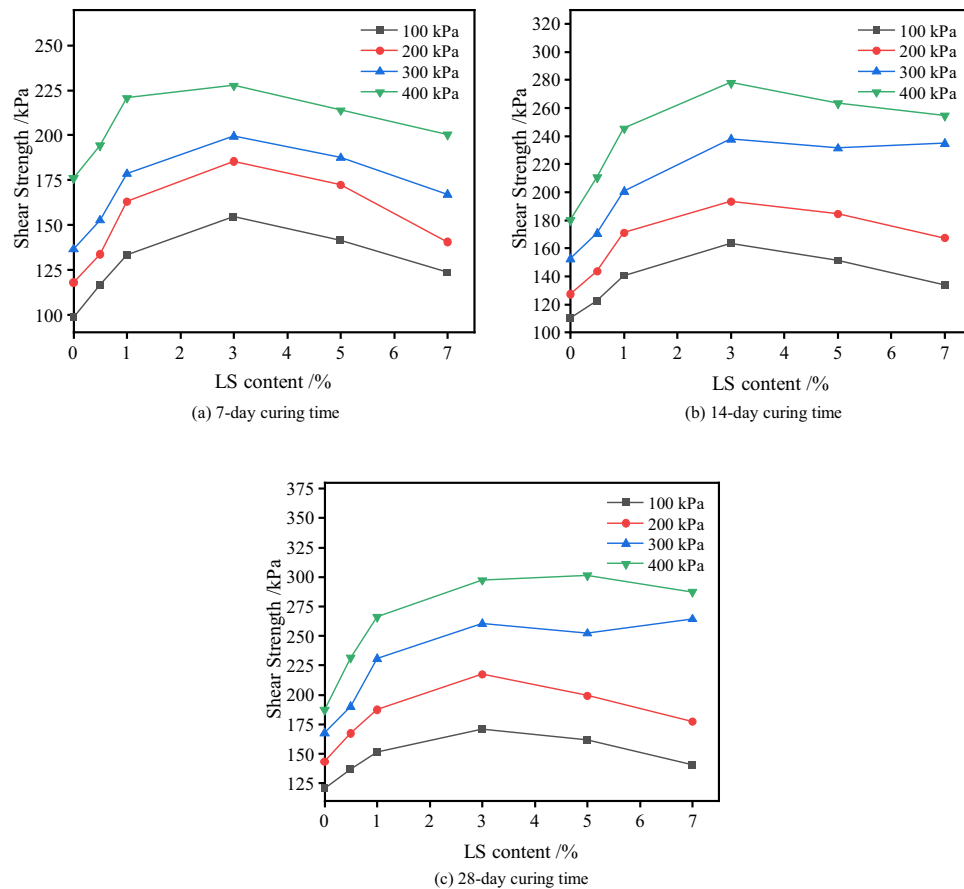


Fig. 5 Effects of LS content on shear strength at curing time of a 7, b 14 and c 28 days



Fig. 6 Direct shearing specimen diagram

time, whereas it increases initially and then decreases with increased LS dosage. The strength reaches the maximum value at 3 wt.% LS content. In Fig. 7a, the UCS value of 28-day curing time substantially increased for all LS-treated red clays, and increased to a maximum of 780.6 kPa at 3 wt.% LS content, showing a significance of about 3.78 times. Figure 7b shows the UCS value of untreated soil is 138.7 kPa at the compaction degree of 97%, and gradually increases with an increase in LS dosage within 3 wt.%. The UCS value of 28-day curing time increased by 3.36 times at 3 wt.% LS content. It is widely recognized that LS acts as cementation in soil particles, connecting them and filling the pores, and bonding LS with the red clay minerals more closely with curing time [45]. However, a gradual decrease in strength was observed with an increase of LS dosage,

which is attributed to the formation of soft surfaces after excess LS aggregation, and the aggregated LS easy slide under the external force, which is macroscopically manifested by a decrease in strength. Thus, it can be inferred that LS substantially enhances the UCS compared to that of natural red clay. A damage diagram of UCS test specimens is shown in Fig. 8.

3.4 Zeta Potential

Changes in the diffusion layer on the surface of the clay particles were analyzed based on the results of the electrophoretic tests. The Gouy-Chapman diffusion bilayer model is shown in Fig. 9 [46] and can quantitatively characterize the thickness change of the diffuse double electric layer, which is significant in studying soil stability.

Under the assumption that the Gouy-Chapman diffusion electric double-layer model is satisfied, the charge density (σ) on the surface of soil particles is calculated by Eq. (1) [47].

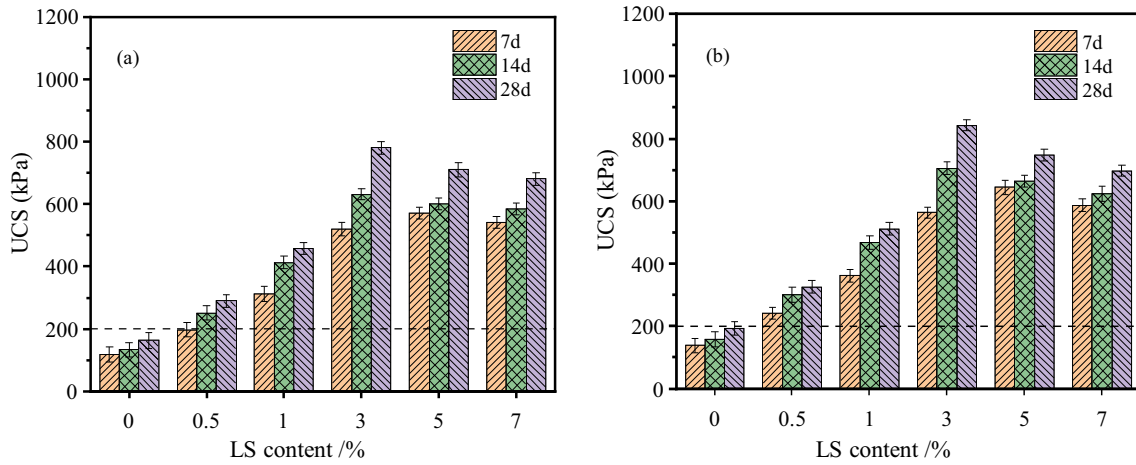


Fig. 7 UCS of red clay at various curing time with different compaction degrees: a 95% and b 97%

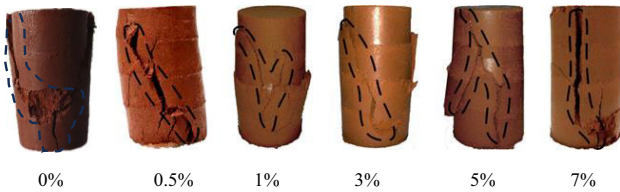


Fig. 8 Damage diagram of UCS test specimen

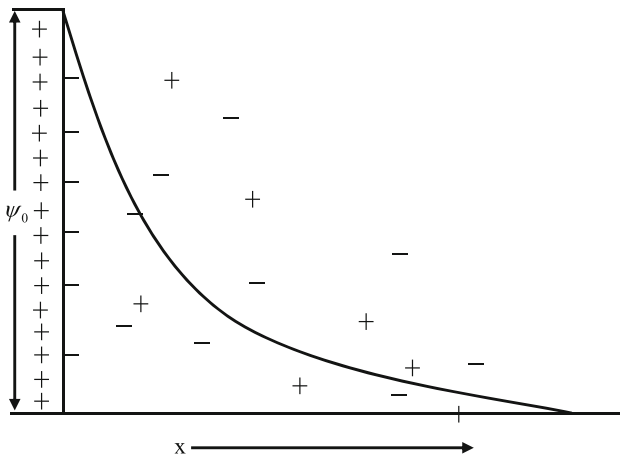


Fig. 9 Gouy-Chapman diffusion double-layer model

$$\sigma = \int_0^\infty \left(\frac{\partial^2 \psi_0}{\partial x^2} \right) dx = \varepsilon \frac{\partial \psi_0}{\partial x} \Big|_{x=0}^{x=\infty} = -\varepsilon \left(\frac{\partial \psi_0}{\partial x} \right)_{x=0} = \varepsilon \kappa \psi_0 \tag{1}$$

where, σ is the charge density on the surface of soil particles, ε is the dielectric constant, κ is the reciprocal of the thickness of the DDL, x is the distance from the surface of soil particles and ψ_0 is the particle surface potential.

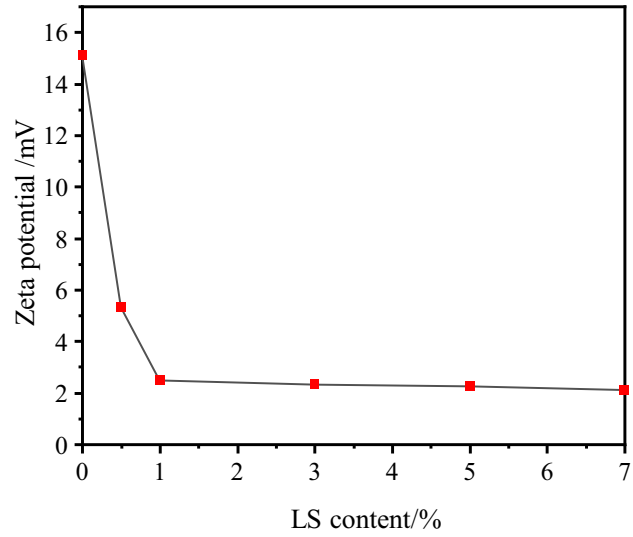


Fig. 10 Zeta potential variation of LS-treated red clay

From Eq. (1), it is seen that κ increases with the growth of electrolyte consistency and charge number, which means that the thickness of the DDL on the surface of the particles (the inverse of κ) becomes smaller as σ increases. In an electrophoresis test of the solution containing deionized water and different LS content, the soil particles with charges on the surface moved towards the electrodes with opposite electrical properties in the electric field. The test results are presented in Fig. 10. As shown in Fig. 10, the zeta potential of red clay decreases with an increase in the LS content, and a decrease in the zeta potential value indicates a decrease or change in the surface charge of the particles. However, from Eq. (1), a positive relationship can be observed between the zeta potential and DDL thickness. The reduction of the diffusion layer causes a decrease in the zeta potential because the LS can interact with the negative charges on the soil particle surface to

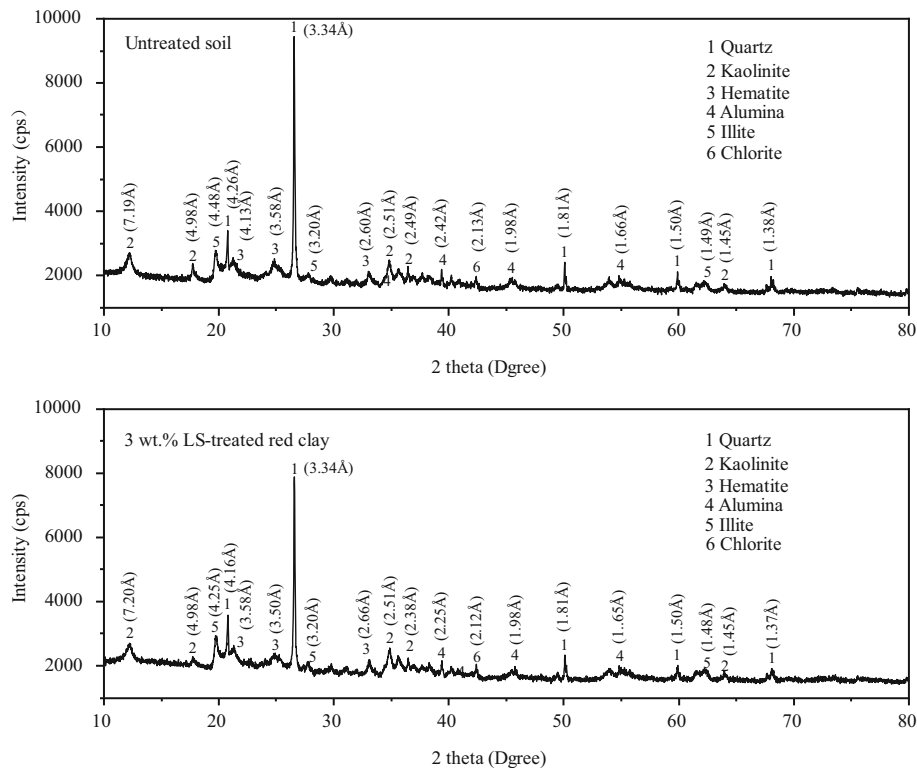


Fig. 11 XRD diffractograms of untreated and 3 wt.% LS-treated red clay

Table 4 Parameters obtained from the XRD analysis of untreated and 3 wt.% LS-treated red clay

Type of clay mineral	Bragg's angle (degrees)	Untreated soil		3% LS-treated red clay		Percentage reduction (%)
		FWHM (degrees)	Crystalline size (nm)	FWHM (degrees)	Crystalline size (nm)	
Quartz	27.81	0.176	48.79	0.266	32.21	34.01
Kaolinite	17.77	0.241	34.93	0.318	26.49	24.16
Hematite	25.45	0.393	21.74	0.498	17.16	21.06
Alumina	45.44	0.395	22.87	0.411	21.98	3.89
Illite	19.77	0.189	44.76	0.289	29.27	34.60
Clinchlore	42.40	0.120	74.51	0.267	33.53	54.99

FWHM full width at half maximum

neutralize some of those charges, which leads to the weakening of the attraction force between soil particles. The thickness of the DDL is reduced and the repulsive force between the particles decreases, contributing to a reduction in boundary moisture content of the LS-treated red clay.

3.5 XRD Analysis

XRD analysis was used to estimate the crystallite size of the clay minerals and to identify the emergence of new

compounds in both LS-treated red clay and untreated soil. The XRD diffractograms of the untreated and LS-treated red clay after 28-day curing are shown in Fig. 11. The analytical results indicate that the principal minerals present in the red clay are quartz and kaolinite, with micro-levels of chlorite and illite. No changes was observed in the diffraction peak of the LS-treated red clay, which is consistent with the results reported by Vinod et al. [48]. The Scherrer equation was used to determine the crystal sizes of these minerals to assess LS-induced modifications to clay minerals in more detail, as shown in Eq. (2) [49].

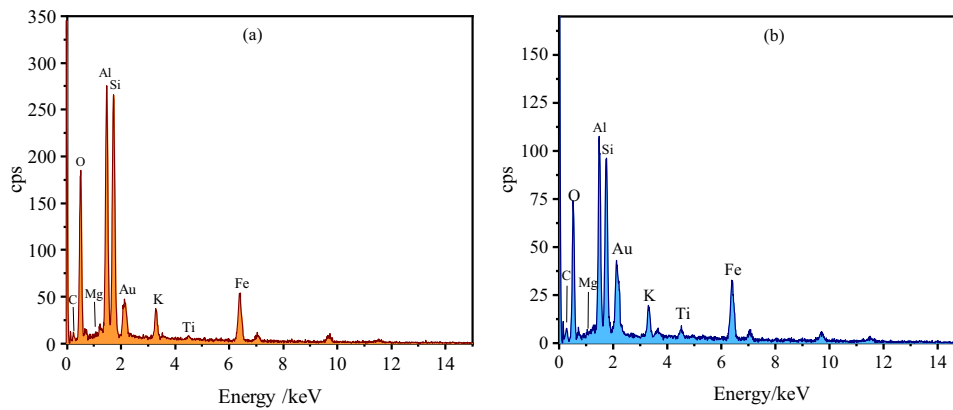


Fig. 12 EDS spectrum of **a** untreated and **b** 3 wt.% LS-treated red clay

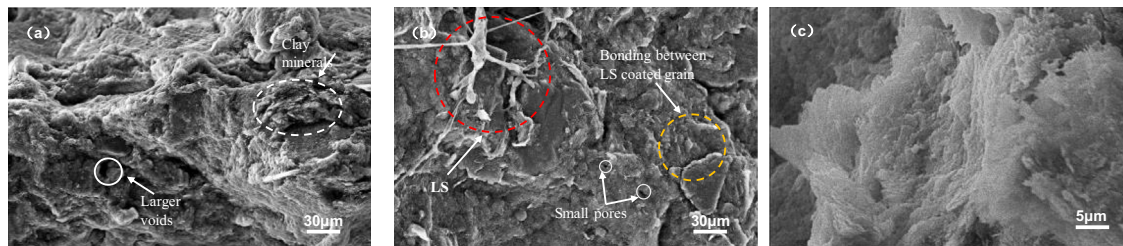


Fig. 13 SEM images of **a** untreated and **b** 3 wt.% LS-treated red clay and **c** LS particles

$$L = \frac{\lambda k}{\beta \cos \theta} \quad (2)$$

where, L = crystalline size; k = Scherrer constant (0.90 in this study); λ = wave length of the X-radiation [λ is 0.15405 nm (1.5405 Å) in this study]; and β = width of a peak at half height expressed in 2θ .

The crystal sizes of red clay mineral are listed in Table 4. It can be noted that the particle sizes of all soil minerals treated with LS decreased compared with untreated red clay, and the crystal size decreased based on the type of clay mineral; the reduction of chlorite can reach up to 54.99%, whereas it was only 3.89% for alumina. This phenomenon could be explained by the interstitial connection between clay minerals and the structure of the clay, which results in bilayers of varying thicknesses [50]. Because no new compounds were discovered, the reduction in mineral crystal size was possibly caused by a change in the negative charge of the clay surface under the action of LS. Consequently, it is inferred that the clay minerals (negatively charged) and LS (positively charged) interact electrostatically, resulting in a decrease in the surface negative charge and a subsequent decrease in the size of the mineral crystal.

3.6 EDS Spectrum

The EDS spectra of original and modified red clay are shown in Fig. 12. As shown in Fig. 12, there was almost no obvious difference in the EDS spectra of the original and modified samples, indicating that no new elements were formed between the red clay and LS. From the perspective of quantitative elemental composition to analysis, the basic constituent elements of clay minerals were Al and Si. If the Al-Si ratio decreases, this indicates that chemical alteration may occur; conversely, this may be because SiO_2 s released from the clay minerals. The Al and Si contents were 17.76% and 15.94% in the untreated soil, respectively, whereas they were 13.22% and 12.44%, respectively, in the LS-treated red clay. The variation in the ratio of Al:Si in this study was approximately 4.39%, which indicates that the variation in the ratio of the elements of the red clay is negligible. Therefore, the slight increase in the ratio from 1.114 to 1.065 after treatment implies that the LS-treated red clay achieves an improvement by altering the mineral lattice without chemical reactions.

3.7 SEM Analysis

To examine the microstructural changes in red clay after LS addition, SEM images of untreated and LS-treated red clay are depicted in Fig. 13. Figure 13a shows that the

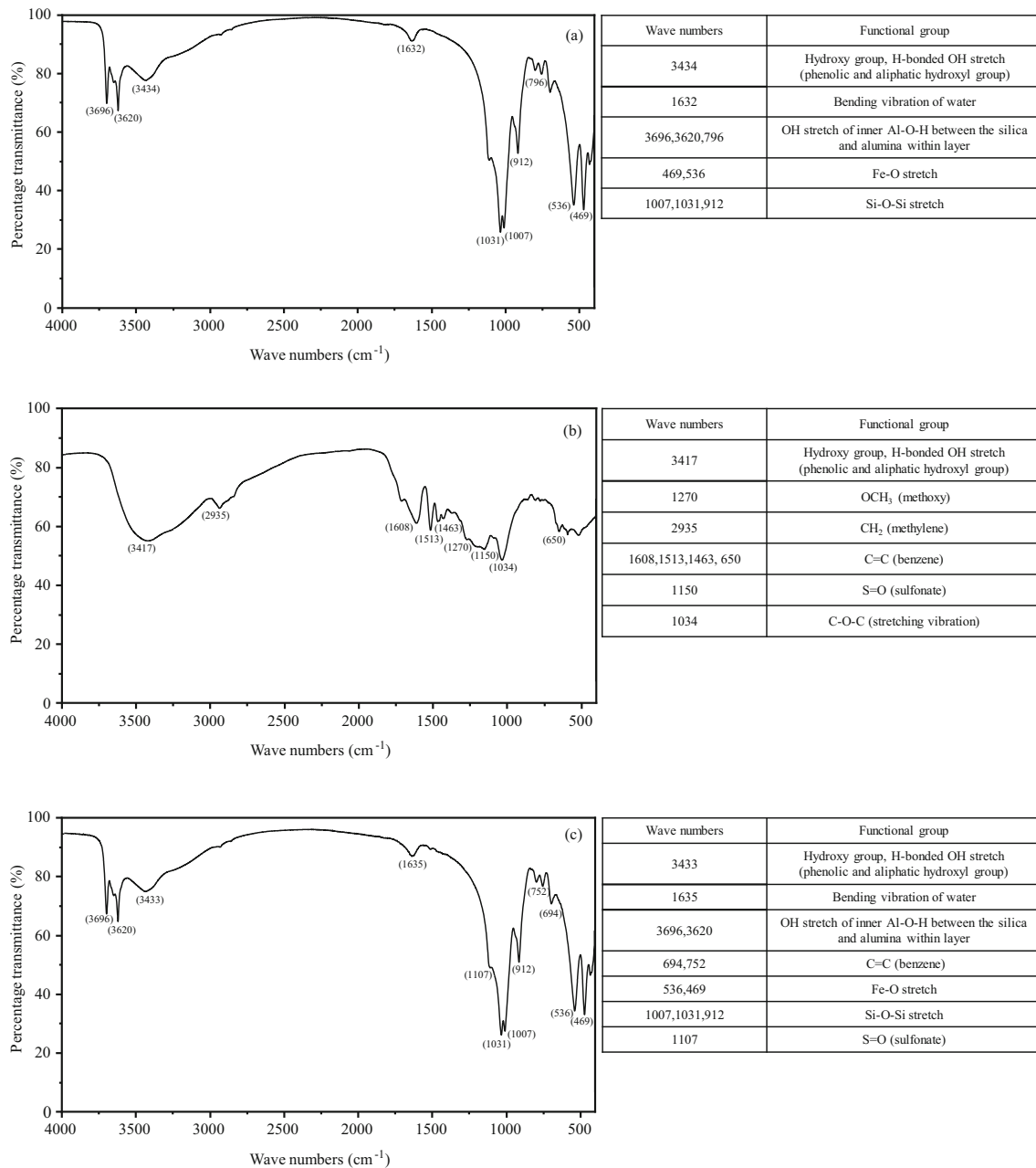


Fig. 14 Functional groups analysis results: **a** red clay, **b** LS, and **c** 3 wt.% LS-treated red clay

untreated red clay structure is discontinuous, composed a loose clay matrix, and has more pores because of the insufficient bonding. The arrangement of the clayey soil mineral sheets can be observed in the upper-right corner of the micrographs in Fig. 13a, which is dominated by face-to-face bonding, and the particle aggregates are predominantly platy and ellipsoidal. In contrast, the SEM images of the 3 wt.% LS treated soil in Fig. 13b showed considerable changes in morphology due to the addition of LS, that is, more sharp-edged flocculated particles can be observed. Red clay particles were coated and bonded with this

cementing material because the interaction between LS and water within the red clay fills the large clay pores and connects small clay particles, resulting in a more stable and aggregated mixture with larger particles. This phenomenon reveals the that pore space was effectively reduced within the red clay, thereby improving the compactness of the soil structure. Hence, the mechanical properties of the red clay improved, which was consistent with the enhancement of the direct shear strength and UCS.

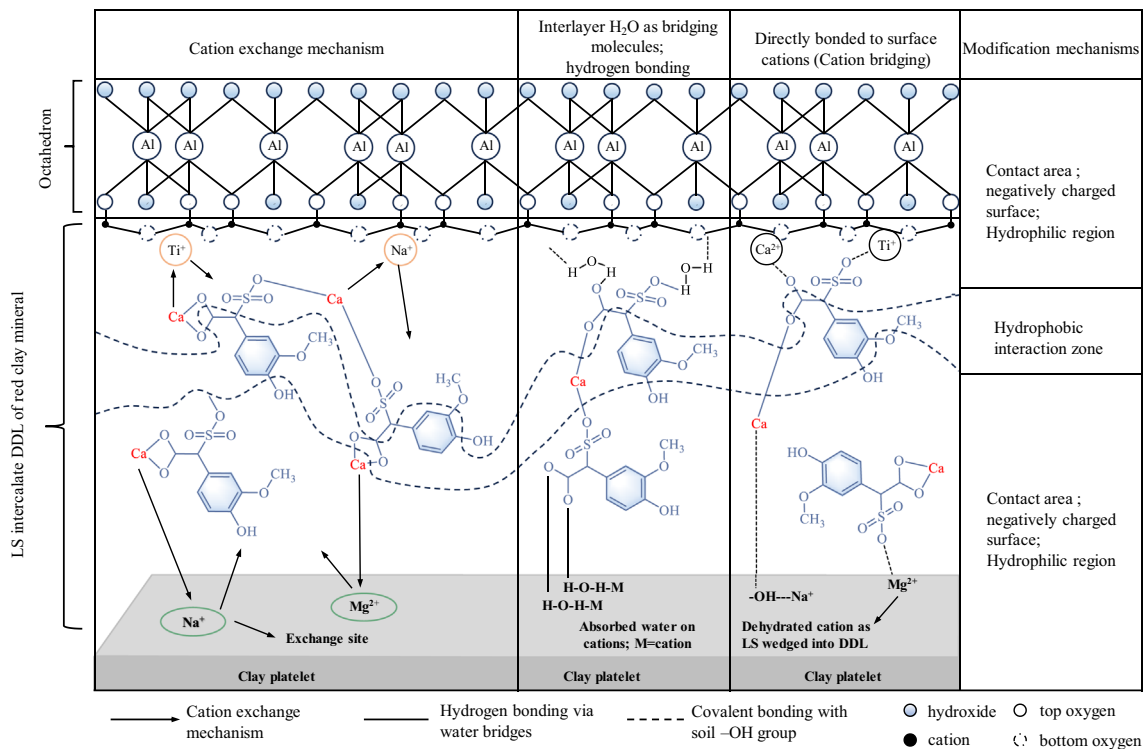


Fig. 15 Modification mechanism of LS on red clay

3.8 FTIR Spectrum

LS is an organic material with complex molecular structure and diverse chemical properties. The chemical properties of organic matter are closely related to the activities of its functional groups. The infrared spectra of the red clay, LS and 3 wt.% LS-treated red clay are depicted in Fig. 14. Figure 14a illustrates that the wider characteristic peaks in the 3700–3100 cm^{-1} range are attributable to the stretching vibration peaks of the hydroxyl group vibration in water adsorbed in the interlayer of the red clay, and the absorption peak at 1632 cm^{-1} is the bending vibration of water. The absorption peaks at 1007 cm^{-1} , 1031 cm^{-1} , and 912 cm^{-1} belong to the stretching vibration of Si–O–Si, whereas the peaks at 3696 cm^{-1} , 3620 cm^{-1} , and 796 cm^{-1} belong to the vibrations of Al–OH, and the peaks at 469 cm^{-1} and 536 cm^{-1} are attributed to the Fe–O vibration. As shown in Fig. 14b, LS mainly contains functional groups consisting of hydroxyl groups (3417 cm^{-1}), benzene ring (1608 cm^{-1} , 1513 cm^{-1} , 1463 cm^{-1} , 650 cm^{-1}), methoxy (1270 cm^{-1}), alkyl groups (2935 cm^{-1}), sulfonic acid groups (1150 cm^{-1}) and C–O–C groups (1034 cm^{-1}). In Fig. 10c LS-treated red clay contains major functional groups of red clay and LS, and the existence of characteristic functional groups like benzene (694 cm^{-1} , 752 cm^{-1}) and S=O (1107 cm^{-1}) are confirmed by additional peaks in comparison with Fig. 14a.

The same was found by Tomás et al. [51] who confirmed the formation of bonds between clay minerals and LS.

3.9 Modification Mechanism of LS

Through a series of instrumental analysis techniques, the changes in the performance of red clay before and after LS doping were evaluated, and the mechanism of the effect of LS on the boundary moisture content of red clay was explored.

Figure 15 shows a schematic illustration of the mechanism of LS-induced changes in the boundary moisture content of the red clay. It can be seen from Fig. 15 that electrostatic interactions, hydrogen bonds and covalent bonds occurred between the red clay and LS, resulting in the adsorption of LS to the soil mineral surface. After the addition of LS to red clay, it is hydrolyzed with soil pore water, and the disintegrated H^+ shares a pair of electrons with the active alcohol hydroxyl group of LS, thus forming positively charged cement in the soil [52, 53]. Owing to electrostatic action, the positively charged cementitious products formed are adsorbed on the surface of the negatively charged clay minerals. This process of electric neutralization changes the structure of the diffuse double electric layer of the soil particles and the thickness of the water film, which is consistent with the changing trends in the zeta potential and clay crystal size. Meanwhile, LS is

embedded in the expansive mineral lattice, displacing water in the outer layer of coordinated monovalent and divalent cations, and then forming direct hydrogen bonds with the coordinated water or covalent bonds with the adsorbed cations in the soil [29]. Soil minerals are wrapped by LS through hydrogen bonds, causing flocculation and agglomeration of the soil, which decreases the specific surface area and densifies thereby enhancing the mechanical properties of the soil [54]. The high-valence cation Ca^{2+} of LS with the low-valence cation (Na^+ , Li^+) on the surface of clay minerals weakens the thickness of the adsorption-bound water layer on the surface of the soil particles, resulting in a decrease in the boundary moisture content and an increase in the attraction between the particles, making the soil structure more stable [44, 55]. Furthermore, the substitution of the cationic end of LS for negatively charged soil particles also reduces the affinity of red clay for water to a certain extent, promoting the flocculation of the particles, enlarging the contact force between the flocculated aggregates, and significantly improving the strength.

4 Conclusions

This study proposes a method for improving red clay with a high liquid content in the southern region of China, which is unsuitable as a roadbed filler in practical construction. Indoor tests were conducted to evaluate the performance and modification mechanism of red clay treated with LS. The main findings of this study are as follows:

- With an increase in the LS dosage, the LL and PI of the red clay initially decreased rapidly and then gradually increased. Moreover, the addition of LS resulted in an LL of less than 50% and a PI below 26, which do not qualify as high-liquid-limit clay, making it suitable for use as roadbed fill.
 - The UCS and direct shear strength of LS-treated red clay initially increased and then decreased as the LS dosage increased. The maximum strength was achieved when the curing age was 28 d, compaction reached 95%, and the LS dosage was 3 wt.%. Under these conditions, the UCS strength and direct shear strength increased by 378.4% and 136%, respectively, compared to the untreated soil. However, excessive LS content caused a decrease in soil strength owing to the agglomeration effect of LS.
 - Microstructural analysis of LS-treated red clay shows that the flocculation substance produced by the interaction between LS and red clay can effectively fill the pores and connect the soil particles, making the modified red clay particles denser and more stable.
- The LS-treated red clay had no new mineralogical components or chemicals generated, and the particle size of each mineral was reduced, indicating a denser mineral composition.
 - The modification mechanism of LS-treated red clay was established using multiple scales. At the fine-scale level, the LS treatment thinned the bilayer of the red clay particles through electrostatic and ion-exchange effects, resulting in a significant reduction in the boundary moisture content of the red clay. Additionally, LS treatment generates flocculating substances that interact with soil minerals, enhancing soil stability and improving mechanical properties.

5 Limitations

The main focus of this study was to investigate the modification effects of LS on red clay widely distributed in southern China. The application of soil under other geological and environmental conditions was not investigated. This study mainly focused on analysing the short-term effects of LS on red clay, and the long-term durability of LS-treated red clay soils under different environmental conditions was not investigated further. In addition, the potential environmental impacts of the production and application of LS have not been explored.

6 Recommendations for Future Research

- (1) To ensure practicality, it is necessary to conduct site-specific tests to determine the optimum curing-agent dosage before applying these findings in engineering practice.
- (2) Further research is needed to ensure its effectiveness for long-term behaviour, possibly by conducting wet-dry and freeze–thaw cycles, as well as discussing the effects of longer curing times on the test specimens.
- (3) Comparison of the constructability and cost-effectiveness of LS with conventional additives is encouraged, taking into account the environmental cost of each additive.

Acknowledgements This work is supported by the Natural Science Foundation of Fujian Province (2022J01091). The authors gratefully acknowledge their financial support.

Funding Natural Science Foundation of Fujian Province (2022J01091).

Data Availability All data, models, and code generated or used during the study appear in the published article.

References

1. Junzhe W, Wu L, Ruoqiang F (2016) An experimental case study of a high-liquid-limit lateritic soil with its application in road construction. *Road Mater Pavement Des.* <https://doi.org/10.1080/14680629.2016.1211031>
2. Zheng L, Ran F, Yulin Z, Hailin Y (2019) Study on the dynamic deformation of road high liquid limit subgrade soil. *Adv Civ Eng.* <https://doi.org/10.1155/2019/4084983>
3. Zeng L, Yu H-C, Gao Q-F, Liu J, Liu Z-H (2022) Evolution of tensile properties of compacted red clay under wet and dry cycles. *KSCE J Civ Eng* 26:606–618. <https://doi.org/10.1007/s12205-021-0527-6>
4. Chen LJ, Chen XJ, Yang X, Bi PY, Ding X, Huang X, Wang H (2020) Effect of calcium carbonate on the mechanical properties and microstructure of red clay. *Adv Mater Sci Eng.* <https://doi.org/10.1155/2020/5298186>
5. Ma HY, Pei CL, Huang RJ, Xu S (2024) Crack evolution and strength attenuation of red clay under dry–wet cycles. *J Mater Civ Eng* 36:04024045. <https://doi.org/10.1061/JMCEE7.MTENG-17190>
6. Liu X, Ke S, Jiang H, Baoning H, Jun-Gao Z (2015) Utilization of high liquid limit soil as subgrade materials with pack-and-cover method in road embankment construction. *Int J Civ Eng.* <https://doi.org/10.22068/ijce.13.3.167>
7. Xi Q, Anchen N, Nan Z, Zhenghao C (2021) Erosion control and growth promotion of w-oh material on red clay highway slopes: a case study in south china. *Sustainability.* <https://doi.org/10.3390/su13031144>
8. Yanzhao Z, Shuangying Z, Rita Yi Man L, Yunchuan M, Guosheng Y, Min Z (2020) Experimental study on the mechanical properties of guiyang red clay considering the meso micro damage mechanism and stress path. *Sci Rep.* <https://doi.org/10.1038/s41598-020-72465-x>
9. JTG D30–2015 (2015) Specifications for design of highway subgrades. China Communication Press, Beijing
10. Qiang M, Zeli H, Hu Z, Junhui L (2022) Strength characteristics and micro-scale mechanism of high liquid limit clay treated by recycled construction and demolition wastes (cdw) aggregates. *Constr Build Mater.* <https://doi.org/10.1016/j.conbuildmat.2022.127367>
11. Ma HY, Duan ZB, Zhang TF, Xu S, Lv MX (2024) Micro-constructive damage model of dry–wet cyclic red clay based on Weibull distribution. *J Test Eval* 52:1095–1108. <https://doi.org/10.1520/JTE20230396>
12. Soltani A, Azimi M, O’Kelly BC (2023) Reappraisal of linear shrinkage test for plasticity index determination and classification of fine-grained soils. *Appl Clay Sci* 238:13. <https://doi.org/10.1016/j.clay.2023.106920>
13. Yousif Ismael M, Ahmed M, Rizgar H, Ahmed MH, Hawkar Hashim I (2021) Modeling and statistical evaluations of unconfined compressive strength and compression index of the clay soils at various ranges of liquid limit. *J Test Eval.* <https://doi.org/10.1520/jte20200505>
14. Vipulanandan C, Ahmed M (2020) Characterizing the index properties, free swelling, stress–strain relationship, strength and compacted properties of polymer treated expansive ch clay soil using vipulanandan models. *Geotech Geol Eng.* <https://doi.org/10.1007/s10706-020-01387-2>
15. Vipulanandan C, Ahmed M (2020) Quantify the effect of temperature on the electrical resistivity, yield stress, and hpht fluid loss of the bentonite-clay drilling mud modified with acrylamide polymer. *J Build Pathol Rehabil.* <https://doi.org/10.1007/s41024-020-00085-z>
16. Vipulanandan C, Ahmed M (2021) Comparison between mohr-coulomb failure criterion and vipulanandan failure models to predict the maximum j_2 invariant and behaviour of clay (ch). *Geomech Geoeng.* <https://doi.org/10.1080/17486025.2021.1980620>
17. Vipulanandan C, Ahmed M (2021) 3-dimension stresses and new failure model to predict behavior of clay soils in various liquid limit ranges. *Arabian J Geosci.* <https://doi.org/10.1007/s12517-021-06553-1>
18. Eduardo Garzón G, Cano MLC, Brendan COK, Pedro JSS (2016) Effect of lime on stabilization of phyllite clays. *Appl Clay Sci.* <https://doi.org/10.1016/j.clay.2016.01.042>
19. Lijie C, Xuejun C, He W, Xiang H, Yun-Jeong S (2020) Mechanical properties and microstructure of lime-treated red clay. *KSCE J Civ Eng.* <https://doi.org/10.1007/s12205-020-0497-0>
20. Ricardo Moreira V, Márcia Maria dos Anjos M, Renato Resende A, Tomásda Rosa S, Renato Batista de O, Marta Pereira da L (2020) Evaluation of lime-treated lateritic soil for reservoir shoreline stabilization. *Water.* <https://doi.org/10.3390/w12113141>
21. Nima L, Amin E, Aminaton M, Christopher LM (2017) Tropical residual soil stabilization: a powder form material for increasing soil strength. *Constr Build Mater.* <https://doi.org/10.1016/j.conbuildmat.2017.04.115>
22. Milene Yumi M, Motomichi K, Hayato N, Osvaldo Mitsuyuki C, Eiji A (2021) Hydrogen-assisted damage evolution in nitrogen-doped duplex stainless steel. *Int J Hydrogen Energy.* <https://doi.org/10.1016/j.ijhydene.2020.10.152>
23. Reginaldo Sérgio P, Fabiano E, Eder Pereira M, Alcides G (2018) Soil stabilization with lime for the construction of forest roads. *Floresta e Ambiente.* <https://doi.org/10.1590/2179-8087.007715>
24. Tao Z, Guojun C, Songyu L (2018) Assessment of mechanical properties in recycled lignin-stabilized silty soil as base fill material. *J Cleaner Prod.* <https://doi.org/10.1016/j.jclepro.2017.12.011>
25. Xiaobo D, Qian W, Qin M, Ye T, Zhang J (2023) Study on strengthening and waterproofing mechanism of calcium lignosulfonate in silty soil sites. *Coatings.* <https://doi.org/10.3390/coatings13081402>
26. Avinash Kumar S, Jagdish Prasad S (2022) Experimental modeling for time-dependent strength behavior of lignosulfonate-treated high plasticity clay. *J Mater Civ Eng.* [https://doi.org/10.1061/\(asce\)mt.1943-5533.0004292](https://doi.org/10.1061/(asce)mt.1943-5533.0004292)
27. Seco A, Francisco R, Miqueleiz L, Beñat G (2011) Stabilization of expansive soils for use in construction. *Appl Clay Sci.* <https://doi.org/10.1016/j.clay.2010.12.027>
28. Hanifi C, Aram A, Fatih C (2015) Soil stabilization of clay with lignin, rice husk powder and ash. *Geomech Eng.* <https://doi.org/10.12989/gae.2015.8.1.067>
29. Alazigha DP, Indraratna B, Vinod JS, Heitor A (2018) Mechanisms of stabilization of expansive soil with lignosulfonate admixture. *Transp Geotech* 14:81–92. <https://doi.org/10.1016/j.trgeo.2017.11.001>
30. Qingsheng C, Buddhima I, John C, Cholachat R (2014) A theoretical and experimental study on the behaviour of lignosulfonate-treated sandy silt. *Comput Geotech.* <https://doi.org/10.1016/j.compgeo.2014.06.010>
31. Zhentao B, Dongbo L, Dong Z, Wei L, Jiaping L (2023) Experimental research on collapsibility of Xi’an loess improved by calcium lignosulfonate. *Coatings.* <https://doi.org/10.3390/coatings13010157>
32. Mariano Tomás F, Sandra O, Mauro C, Teresa María P, Diego M (2021) Performance of calcium lignosulfonate as a stabiliser of highly expansive clay. *Transp Geotech.* <https://doi.org/10.1016/j.trgeo.2020.100469>

33. ASTM D2487–17e1 (2017) Standard practice for classification of soils for engineering purposes (unified soil classification system). ASTM Int West Conshohocken, PA. <https://doi.org/10.1520/D2487-17E01>
34. Fernandez MT, Orlandi S, Codevilla M, Piqué TM, Manzanal D (2021) Performance of calcium lignosulfonate as a stabiliser of highly expansive clay. *Transp Geotech* 27:100469–100469. <https://doi.org/10.1016/j.trgeo.2020.100469>
35. ASTM D4318–17e1 (2017) Standard test methods for liquid limit, plastic limit, and plasticity index of soils. ASTM Int West Conshohocken, PA. <https://doi.org/10.1520/D4318-17E01>
36. Cai GJ, Zhang T, Liu SY, Li JH, Jie DB (2016) Stabilization mechanism and effect evaluation of stabilized silt with lignin based on laboratory data. *Mar Georesour Geotec* 34:331–340. <https://doi.org/10.1080/1064119X.2014.966217>
37. Sarker D, Apu OS, Kumar N, Wang JX, Lynam JG (2023) Sustainable lignin to enhance engineering properties of unsaturated expansive subgrade soils. *J Mater Civ Eng*. <https://doi.org/10.1061/jmcee7.mteng-15008>
38. ASTM D3080-04 (2012) Standard test method for direct shear test of soils under consolidated drained conditions. ASTM Int West Conshohocken, PA. <https://doi.org/10.1520/D3080-04>
39. ASTM D2166-06 (2016) Standard test method for unconfined compressive strength of cohesive soil. ASTM Int West Conshohocken, PA. <https://doi.org/10.1520/D2166-06>
40. ASTM E2865-12 (2022) Standard guide for measurement of electrophoretic mobility and zeta potential of nanosized biological materials. ASTM Int West Conshohocken, PA. <https://doi.org/10.1520/E2865-12R22>
41. ASTM E2860-20 (2021) Standard test method for residual stress measurement by x-ray diffraction for bearing steels. ASTM Int West Conshohocken, PA. <https://doi.org/10.1520/E2860-20>
42. ASTM E986-04 (2017) Standard practice for scanning electron microscope beam size characterization. ASTM Int West Conshohocken, PA. <https://doi.org/10.1520/E0986-04R17>
43. ASTM E3085-17 (2022) Standard guide for fourier transform infrared spectroscopy in forensic tape examinations. ASTM Int West Conshohocken, PA. <https://doi.org/10.1520/E3085-17>
44. Dong C, Huang Y, Zhang W, Tang X, Gu Y, Feng Y (2023) Behavioral evaluation on the engineering properties of lignin-stabilized loess: reuse of renewable materials. *Constr Build Mater* 369:130599–130599. <https://doi.org/10.1016/j.conbuildmat.2023.130599>
45. Vakili AH, Salimi M, Yang L, Shamsi M, Nazari Z (2022) Strength and post-freeze-thaw behavior of a marl soil modified by lignosulfonate and polypropylene fiber: an environmentally friendly approach. *Constr Build Mater* 332:127364–127364. <https://doi.org/10.1016/j.conbuildmat.2022.127364>
46. Tripathy S, Sridharan A, Schanz T (2004) Swelling pressures of compacted bentonites from diffuse double layer theory. *Can Geotech J* 41:437–450. <https://doi.org/10.1139/t03-096>
47. Bharat TV, Sridharan A (2015) Prediction of compressibility data for highly plastic clays using diffuse double-layer theory. *Clays Clay Miner* 63:30–42. <https://doi.org/10.1346/ccmn.2015.0630103>
48. Vinod JS, Indraratna B, Mahamud MA (2010) Stabilisation of an erodible soil using a chemical admixture. *Proc Inst Civ Eng* 163:43–51. <https://doi.org/10.1680/grim.2010.163.1.43>
49. Drits VA, Środoń J, Eberl DD (1997) Xrd measurement of mean crystallite thickness of illite and illite/smectite: reappraisal of the kubler index and the scherrer equation. *Clays Clay Miner* 45:461–475. <https://doi.org/10.1346/ccmn.1997.0450315>
50. Zhang T, Cai G, Liu S (2018) Application of lignin-stabilized silty soil in highway subgrade: a macroscale laboratory study. *J Mater Civ Eng*. [https://doi.org/10.1061/\(ASCE\)MT.1943-5533.0002203](https://doi.org/10.1061/(ASCE)MT.1943-5533.0002203)
51. Mariano Tomás F, Sandra O, Mauro C, Teresa María P, Diego M (2021) Performance of calcium lignosulfonate as a stabiliser of highly expansive clay. *Transp Geotech* 27:100469–100469. <https://doi.org/10.1016/j.trgeo.2020.100469>
52. Mengistu W, Fassil K, Bobe B, Emiru B (2018) Effect of community-based soil and water conservation practices on soil glomalin, aggregate size distribution, aggregate stability and aggregate-associated organic carbon in northern highlands of Ethiopia. *Agric Food Secur*. <https://doi.org/10.1186/s40066-018-0193-1>
53. Xiumei Z, Yuxin L, Qian W, Jinlian M, Shouyun L, Yan W, Xiaowei X (2022) Evaluation and analysis of the effect of lignin amelioration on loess collapsibility. *J Renewable Mater* 10:3405. <https://doi.org/10.32604/jrm.2022.021120>
54. Johannes L, James K, Daniel S (2007) Organic matter stabilization in soil microaggregates: implications from spatial heterogeneity of organic carbon contents and carbon forms. *Biogeochemistry* 85:45–47. <https://doi.org/10.1007/s10533-007-9105-3>
55. Yang JY, Guo YC, Shen AQ, Fan JT, Qi HZ, Lyu ZH, He ZM (2023) Mechanics, durability, and reinforcement mechanism of red clay soils stabilized by the consolid system. *J Mater Civ Eng*. [https://doi.org/10.1061/\(ASCE\)MT.1943-5533.0004634](https://doi.org/10.1061/(ASCE)MT.1943-5533.0004634)

Springer Nature or its licensor (e.g. a society or other partner) holds exclusive rights to this article under a publishing agreement with the author(s) or other rightsholder(s); author self-archiving of the accepted manuscript version of this article is solely governed by the terms of such publishing agreement and applicable law.